Applied Surface Science 598 (2022) 153702

Contents lists available at ScienceDirect

Applied Surface Science

journal homepage: www.elsevier.com/locate/apsusc

Full Length Article

Self-cleaning and anti-fouling superhydrophobic hierarchical ceramic surface synthesized from hydrothermal and fluorination methods

Mohd Haiqal Abd Aziz [a,b,c], Mohd Hafiz Dzarfan Othman [a,*], Jason R. Tavares [d], Mohammad Arif Budiman Pauzan [a], Mizuki Tenjimbayashi [e], Ang Wei Lun [c], Nur Hashimah Alias [f], Ahmad Fauzi Ismail [a], Mukhlis A Rahman [a], Juhana Jaafar [a]

[a] Advanced Membrane Technology Research Centre (AMTEC), School of Chemical and Energy Engineering (FCEE), Universiti Teknologi Malaysia, 81310 UTM Skudai, Johor, Malaysia
[b] Department of Chemical Engineering Technology, Faculty of Engineering Technology, Universiti Tun Hussein Onn Malaysia, Pagoh Higher Education Hub, 84600 Panchor, Johor, Malaysia
[c] Fakulti Kejuruteraan dan Alam Bina, Universiti Kebangsaan Malaysia, Malaysia
[d] CREPEC, Department of Chemical Engineering, Polytechnique Montreal, Montreal, QC H3C 3A7, Canada
[e] International Center for Materials Nanoarchitectonics (MANA) National Institute for Materials Science (NIMS) 1-1 Namiki, Tsukuba, Ibaraki 305-0044, Japan
[f] Oil and Gas Engineering, School of Chemical Engineering, Universiti Teknologi MARA, Shah Alam, Malaysia

ARTICLE INFO

Keywords:
Superhydrophobic
Ceramic
Hierarchical
Gasphilic
Micro/nanotechnology

ABSTRACT

In this work, we develop superhydrophobic ceramic surfaces possessing flower-like hierarchical structures that can resist surface wetting against not only water but also ethylene glycol and palm oil. This can benefit a wide range of potential applications in many ceramic fields. The synergistic strategy to fabricate superhydrophobic ceramic surfaces relies on the construction of hierarchical structures through pre-roughening. Using TiO_2 microflowers obtained via a hydrothermal approach and post-fluorinating via surface grafting with 1H,1H,2H,2H-perfluorodecyltriethoxysilane (C8) resulted in better metastable Cassie-Baxter state as water droplet roll-off the surface compared to non-textured ceramic surfaces where the water droplet pinned. The C8-TiO_2-modified ceramic surface (C8/TiO_2-CRM) can still maintain a high contact angle against palm oil (above nearly 120°) within 40 min of exposure, whereas the un-textured ceramic surface is fully wetted. In addition, the C8/TiO_2-CRM has excellent self-cleaning, anti-fouling and "gasphilic" properties. In this work, the robustness of the composite interface from hierarchical structures resulting from TiO_2 micro-flowers is further explained.

1. Introduction

To date, research on surfaces that have superhydrophobic property has gained great momentum in response to the need for antiwetting and antifouling properties [1–6]. In general, super-hydrophobic surfaces exhibit water contact angles above 150° and contact angle hysteresis lower than 10° [7,8]. Contact angle hysteresis is related to the resistance to the droplet movement along a solid surface. Surface wettability is frequently distinguished by hysteresis, with lower hysteresis values (necessary below 10°) indicating Cassie-Baxter state and higher hysteresis values indicating Wenzel state. The surface does not allow liquid penetration in the Cassie-Baxter state due to trapped air beneath the droplet and the solid substrate, which is required to create high liquid droplet mobility. Meanwhile, in the Wenzel state, liquid penetration in the roughness surfaces is visible, resulting in a pinning effect [9].

Surface chemistry and surface roughness govern a surface's wettability. Low surface energy materials have played an important role in increasing the hydrophobicity of a surface because, due to their nonpolar chemistries and closely packed and stable atomic structures, they can reduce the intermolecular forces and adhesive force of a surface. [10]. The reactive molecules used in literature for low surface energy modification of surfaces are carbohalogen compounds [11], hydrocarbon compounds [12], fluorosilane compounds [13], organosilicon compounds [14], silsesquioxanes [15], or their combinations. Fluorocarbons have the lowest surface energy due to fluorine's smaller atom size and low polarizability, both of which have a strong influence on their bonding and electronic properties [10]. Because of fluorine's limited polarizability, van der Waals interactions between fluorinated

* Corresponding author.
E-mail address: hafiz@petroleum.utm.my (M.H.D. Othman).

https://doi.org/10.1016/j.apsusc.2022.153702
Received 23 February 2022; Received in revised form 10 May 2022; Accepted 13 May 2022
Available online 23 May 2022

chains are weak, resulting in fluorocarbons with a low cohesive energy [10]. As a result, fluorosilane compounds or fluorinated polymers/co-polymers have emerged as the logical choice for low surface energy materials used in the design of superhydrophobic materials. Despite CF_3 having the lowest surface energy of any chemical group, the highest reached contact angle of a smooth surface using CF_3 is about 120°, which does not meet the requirement for superhydrophobicity unless surface roughness is introduced.

Aside from chemical composition and surface roughness, hierarchical structure should also be considered in the development of a much more stable Cassie-Baxter. The Cassie-Baxter state is favored over the Wenzel state as the number of texture scales increases. [16,17]. In general, most surface structures in nature are hierarchical, which means that more than one scale of texture is used to keep adhesion force low enough for droplets on lotus leaves to roll freely and water striders to walk on water. [18]. A hierarchically structured surface is typically composed of a nanoscale texture on top of a microscale texture [19]. The complementary roles of the microstructure and nanostructure can increase the composite's apparent contact angle while decreasing its sliding contact angle. [20,21]. This is due to the fact that air is trapped at multiple length scales for a hierarchically textured surface, as opposed to only one length scale for a single-tiered textured surface. This means that the solid-liquid contact area for hierarchically textured surfaces is reduced even further, lowering the likelihood of droplet pinning [22].

Superhydrophobic surfaces can effectively trap air between microstructures underwater, resulting in gaseous plastron formation. This air layer has shown great potency in many fields such as membrane distillation [23], membrane contactor [24], carbon capture [25], battery technology [26], electrocatalytic reduction [27] and so-forth. However, recent advances in superhydrophobic modification have focused on polymeric [28,29], metal [30,31] and textile substrates [32,33]. Despite successful modifications, the methods may not be suitable for use in conditions requiring ceramic-based materials. Superhydrophobic ceramic substrates appear to be more robust materials suitable for harsh condition applications because they provide substrates with high thermal, chemical, and mechanical stabilities. Our previous research introduced flower-like structures on the surface of a ceramic hollow fibre membrane, followed by fluorination, which revealed the formation of a shiny air cushion trapped on the surface when immersed in water [34]. Hierarchical roughness from the texture increased the value of the energy barrier, which in turn lead to an improvement of the anti-wetting and anti-fouling properties of the composite surfaces compared to the primary roughness from the grains and pores of fluorinated pristine membrane. The implementation of hydrothermal treatment followed by fluorination for superhydrophobicity is expected to be less complex because it integrates the multiple steps normally required to deposit a nanoscale texture on an underlying coarser length scale structure.

In line with our previous work, we present here a theoretical study that estimates the robustness of the composite interface (1H,1H,2H,2H-perfluorodecyltriethoxysilane-coated TiO_2 microflowers) developed via hydrothermal and fluorination treatments, based on two design parameters: the robustness angle (T*) and the robustness angle height (H*). The design parameters were previously explained in detail in the existing literature [35]. Moreover, we further explore explain in detail the morphology and chemistry of such coatings on a ceramic substrate. We also evaluate the Cassie state stability of the coating using not only water but also low surface tension liquids such ethylene glycol and palm oil. Anti-fouling, self-cleaning and "gasphilic" properties were also evaluated.

2. Experimental

2.1. Materials

Ball clay was purchased from Zibo All Way Import & Export Co., Ltd, China. 1H,1H,2H,2H-perfluorodecyltriethoxysilane (97%) or C8 with a chemical formula of $C_8F_{17}C_2H_4Si(OC_2H_5)_3$ and Titanium (IV) butoxide with a chemical formula of $Ti(C_4H_9O)_4$ were supplied by Sigma-Aldrich. Hydrochloric acid (HCl) fuming 37% and anhydrous ethanol was purchased from Merck. Ethylene glycol was obtained from QRëC™. Palm oil was obtained from Saji Malaysia.

2.2. Ceramic substrate

For the fabrication of the ceramic substrate, ball clay powder was compressed in a home-built press to cylindrical pellets of about 13 mm diameter and 0.4 g weight. Then, the samples were sintered in a muffle furnace (Nabertherm, Germany), under the following sintering profile: the compressed ceramic samples were first sintered from room temperature to 1300 °C at a rate of 5 °C/min and were held at that temperature for 5 h for consolidation. It was then cooled down to 25 °C at 5 °C/min.

2.3. Hydrothermal synthesis of TiO_2 microflowers

The ceramic substrate was placed at the bottom of a Teflon-line stainless steel autoclave containing a mixture of titanium butoxide, HCl and RO water (see Fig. 1(ai)). This method utilizes a metal die to press the dry or slightly humid powders into compacted disk to form small disk ceramic membrane [23]. The solution was made by combining 120 mL of HCl with 120 mL of RO water, then adding titanium butoxide (6 mL) dropwise. Hydrothermal synthesis was carried out at elevated temperature at 150 °C for 10 h to grow the TiO_2 microflowers [34,36]. The reaction during hydrothermal synthesis of TiO_2 microflowers is shown in Fig. 1(b). After the reaction was finished, the autoclave was cooled to room temperature. The TiO_2 modified ceramic substrates were collected and flushed with RO water, followed by drying in ambient air.

2.4. Fluorination

Fluorination was used to impart superhydrophobicity to the substrate after it had been surface roughened with TiO_2 particles. The fluorination procedure was in accordance with the method from previous studies [37,38] where a 2 wt% C8 solution was prepared by adding C8 dropwise into ethanol with continuous mixing. TiO_2-modified ceramic substrates were first hydroxylated in an ethanol/water (1/2 vol/vol) solution for 24 h. After drying, the substrates were immersed in 2 wt% C8 and kept there for 24 h. The reaction mechanism of C8 grafting is shown in Fig. 1(c). Then, the modified substrates were rinsed with ethanol to remove excess C8 and allowed to dry at 60 °C in an oven overnight.

2.5. Characterization

The surface and cross-section morphology of the sintered ceramic was examined using a field emission scanning electron microscope, FESEM (SU8020, Hitachi) and scanning electron microscope, SEM (TM3000, Hitachi) and the samples were sputter-coated with platinum. The FESEM micrographs of both surface and cross-sectional of samples were taken at different magnifications. Attenuated total reflectance-Fourier-transform infrared spectroscopy, ATR-FTIR (Nicolet iS10, Thermo Scientific) was used to examine the surface chemistry of TiO_2 microflowers, C8 and ceramic substrate. The surface topologies were investigated by scanning a 5 mm × 5 mm area with an atomic force microscopy, AFM (5100 N, Hitachi) in the tapping mode. The roughness profile provided by the AFM5000 II software was used to calculate an arithmetic mean of the surface roughness (Ra). X-Ray photoelectron spectroscopy, XPS (Kratos, AXIS Ultra) was used to characterize the surface coating layer of ceramic substrate. The surface wettability of the samples was measured using a goniometer (DataPhysics Instruments, OCA series) at room temperature (25 °C) using contact angles of water

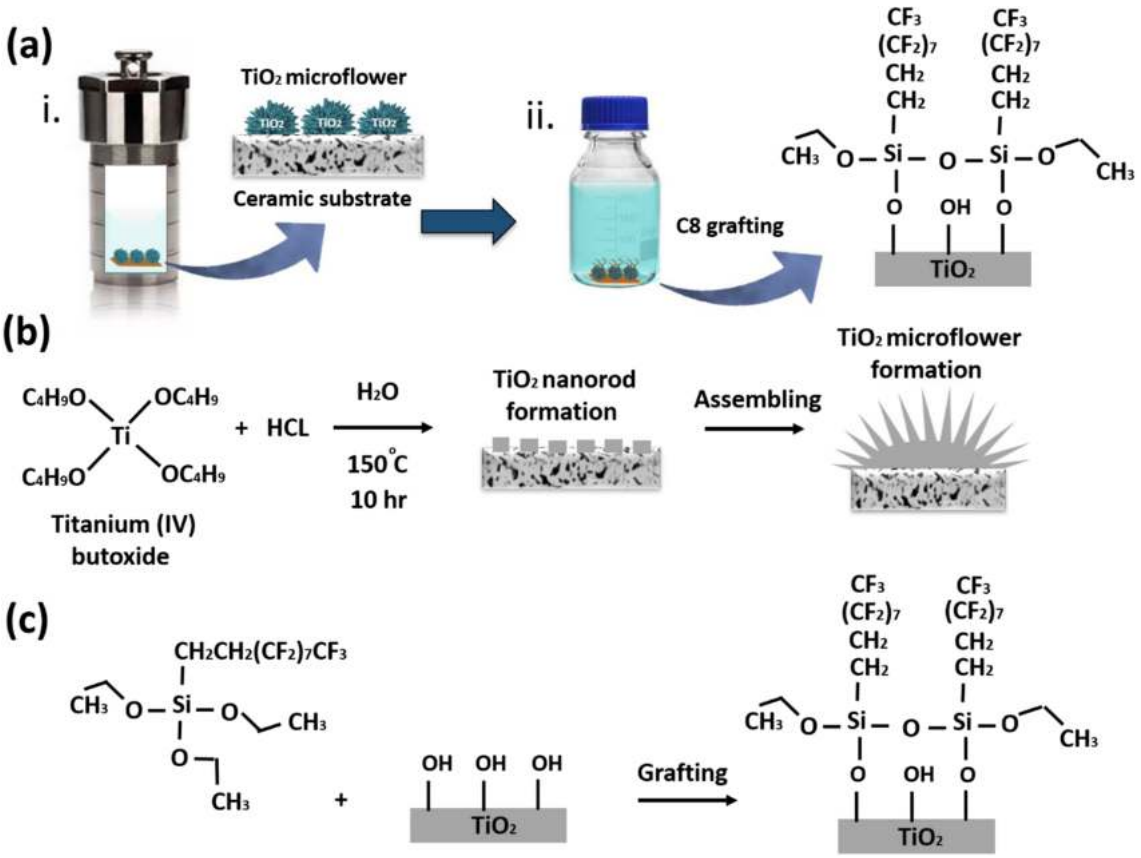

Fig. 1. Schematic illustration of (a) hydrothermal synthesis of TiO_2 microflowers and fluorination method, (b) reaction mechanism of TiO_2 microflowers and (c) post-fluorinating with 1H,1H,2H,2H-perfluorodecyltriethoxysilane.

and low surface tension liquids. One μL of liquid was dropped onto ceramic surface and the contact angle was captured by a high-speed camera promptly. The advancing and receding contact angles were measured by increasing and decreasing the drop volume by 1 μL, respectively. At least three measurements were made to obtain an average value and a standard deviation. Two low surface tension liquids were used, namely ethylene glycol and palm oil, with surface tensions of 47.3 and 28.6 mN/m, respectively [39,40]. The surface tension of water is 72.8 mN/m.

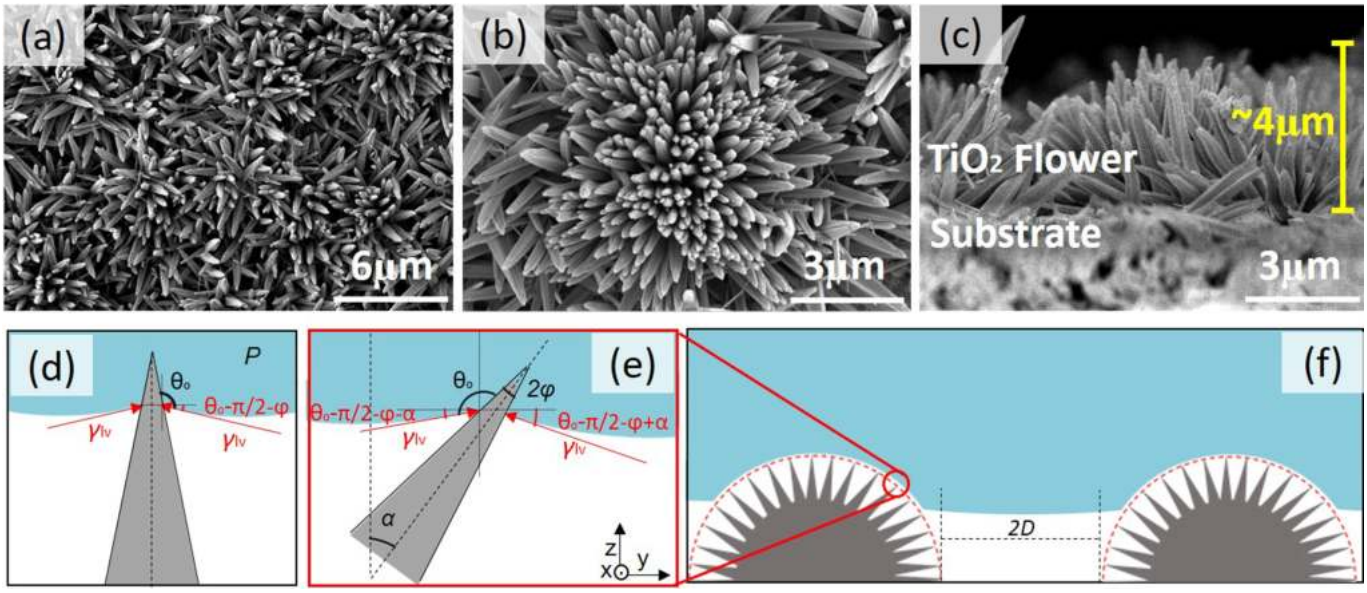

Fig. 2. (a-b) FE-SEM images of surface and (c) cross-section of C8/TiO_2-CRM (d-f) basis of the design parameter of the composite interface, (d-e) having cone-like nanorod as an individual spine and (f) forming acicular network to form microflowers.

3. Results and discussion

3.1. Structural and robustness study

TiO_2 microflower particles were grown on ceramic substrates by both hydrolysis and condensation reaction from titanium (IV) butoxide at 150 °C. The TiO_2 layer evolved different microstructures depending on the hydrothermal reaction time. At 10 h of synthesis time, the surface of the ceramic substrate is uniformly covered with TiO_2 microflowers as can be seen in Fig. 2(a), parallel to our previous work's morphology [34]. During the hydrothermal process, Cl^- played a crucial role in the formation of flower-like structures (this mechanism has been discussed elsewhere [41]). To provide a direct measure of the robustness composite, the structure parameters was evaluated based on FESEM images through ImageJ analysis. As shown in Fig. 2**(b-c)**, TiO_2 micro-flowers are composed of packed nanocrystals that are shaped like cone. The nanorods radiate in an acicular network of very high density, forming a flower-like topography. Considering an acicular framework of TiO_2 micro-flower, the range of the tilt angle (α) of nanorod arrays is estimated from −90° to +90° normal to the membrane surface (basis Fig. 2 **(c-f) and Fig. S1**). The oriented nanorod arrays of the microflowers has an estimated length of 4 μm and an average opening angle (φ) of 11.10° ± 2.3 (**see** Fig. 2(c) **and Fig. S2** respectively).

The obtained flower-like textured surface after being chemically modified with C8 shows good hydrophobicity as evidence by the high static contact angle (159.8° ± 1.5) and the low contact angle hysteresis (0.5° ± 0.6), as shown in Figs. 3**(a,d) and** 4**(a)**. The fluorinated ceramic substrate with hierarchical TiO_2 microflowers, which is denoted as C8/TiO_2-CRM, displays super-hydrophobic and slippery behavior as shown in Fig. 4(c). Meanwhile, the fluorinated ceramic substrate without the secondary structure of TiO_2 (C8-CRM) exhibited lower static contact angle (136.6° ± 3.4) and higher contact angle hysteresis (14.1° ± 6), resulting in strong pinning effects (see Fig. 4(d)). Hierarchical structures from TiO_2 micro-flowers as well as low surface energy from fluorinated material have demonstrated synergistic effects towards forming a Cassie-Baxter surface on C8/TiO_2-CRM. The flower-like hierarchical surface exhibited a Cassie-Baxter state after fluorination. Meanwhile, a Wenzel state was observed on the fluorinated pristine surface with primary structure of pores and grains (see **Fig. S3**). In fact, the C8/TiO_2-CRM surface was able to keep the ethylene glycol hysteresis contact angle below 10° (see Fig. 4(b)), compared to the untextured substrate where it was 30°. As for TiO_2 microflower presence of hierarchical structures, the existence of dense nano-rod arrays can dramatically reduce the solid– liquid surface fraction and minimize the adhesion between solid and liquid surfaces due to multiple energy barriers. To justify our hypothesis, theoretical studies based on the robustness angle (T*) and robustness height (H*) were carried out to quantify the sagging of the liquid-vapor interface as consequences of pressure difference at the interface.

3.2. Robustness angle

The robustness angle (T*) and height (H*) are two parameters that were proposed by Tuteja's group to estimate the robustness of a composite interface [35]. T* provides a dimensionless measure of the pressure (P_θ) required to force the sagging angle, $\delta\theta$, of the vapour-liquid interface to reach the bottom of a composite surface, and H* provides a dimensionless measure of the pressure (P_H) required to force the sagging height, h_1, for the liquid-vapour interface to reach the maximum depth of a composite, h_2 as illustrated in **Fig. S4**. However, the rational design of the composite interface of this work is explained by the cone geometry-like nanorod with an opening angle (φ). The nanorods radiate from its center of gravity, forming an acicular network, where each of the nanorods is tilted in a certain angle (α) (see Fig. 2**(d-f)**) The basis of the parameters (φ and α) for an acicular geometry (see **Fig. S5**) was suggested by Yamauchi et al [42]. Taking those considerations into account, the T* for TiO_2 microflower in this work can be re-written as:

$$T^* = \frac{2L_{cap}cos\alpha \ \ sin(\theta - (\frac{\pi}{2} + \varphi)_{min})}{D} \quad (1)$$

where L_{cap} is the capillary length of the fluid and D is the spacing between the solid textures. The values of φ and α were estimated using a scanning electron microscope and then processed using the ImageJ program (see **Fig. S2 and Table S1**). θ_o is defined as the contact angle of a smooth surface where its surface chemistry is C8 (since C8 was applied on both the C8-CRM and C8/TiO_2-CRM).

Since L_{cap} and D are always positive [42], the evaluation of T^* can be done by plotting T^* relatively to φ, α and θ_o. The derivation of Equation (1) can be seen from supplementary data (from Equation S1 to S11). Fig. 5**(a-b)** shows the theoretical analysis of the effect of α and φ relative to T* from Equation (1). Half opening angles of 6° – 17° for the tip of the

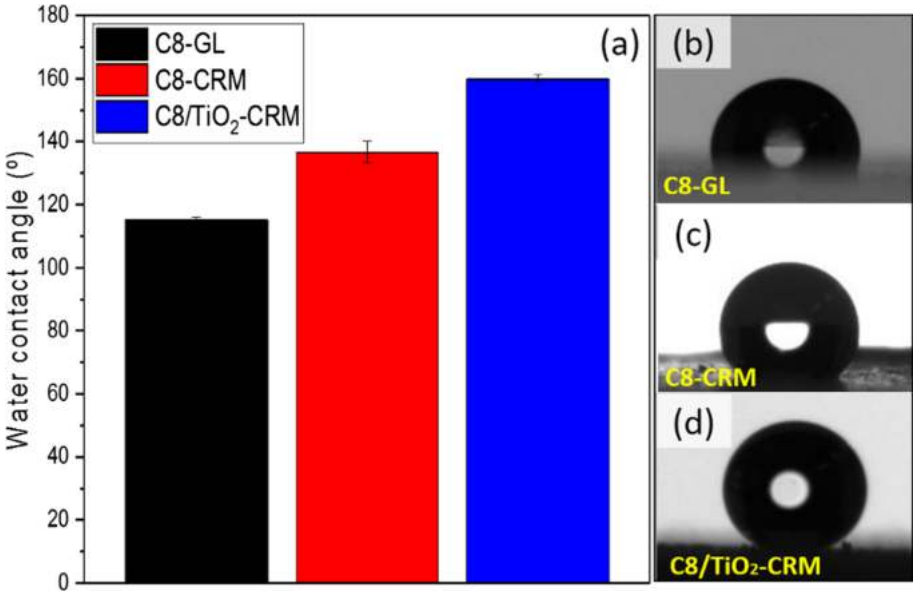

Fig. 3. (a) Static water contact angle for C8 modified smooth glass (C8-GL), C8-CRM and C8/TiO_2-CRM, and adhesion water droplet test on (c) C8/TiO_2-CRM and (d) C8-CRM.

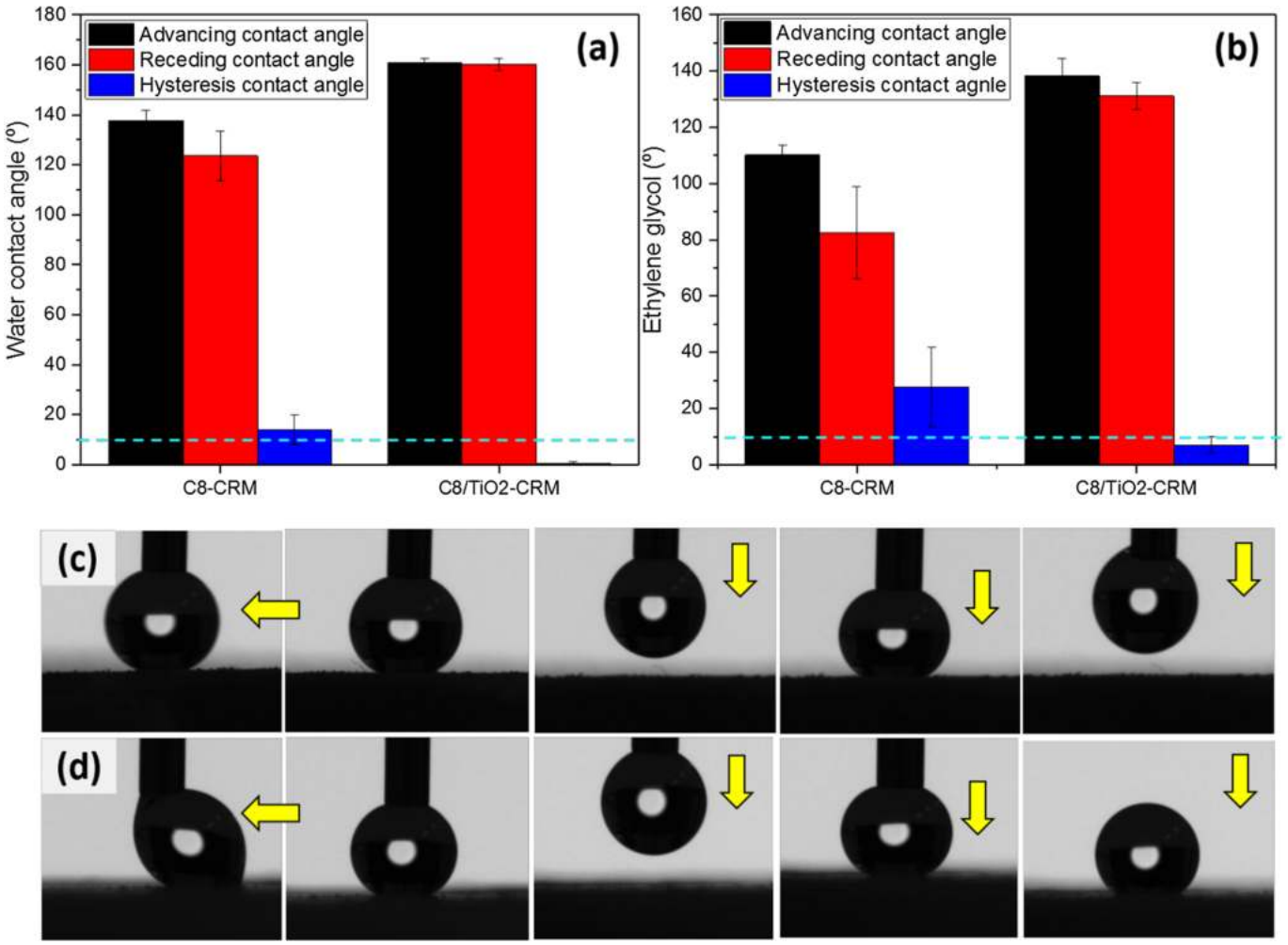

Fig. 4. (a) Water and (b) ethylene glycol contact angle for C8-CRM and C8/TiO_2-CRM, and adhesion water droplet test on (c) C8/TiO_2-CRM and (d) C8-CRM.

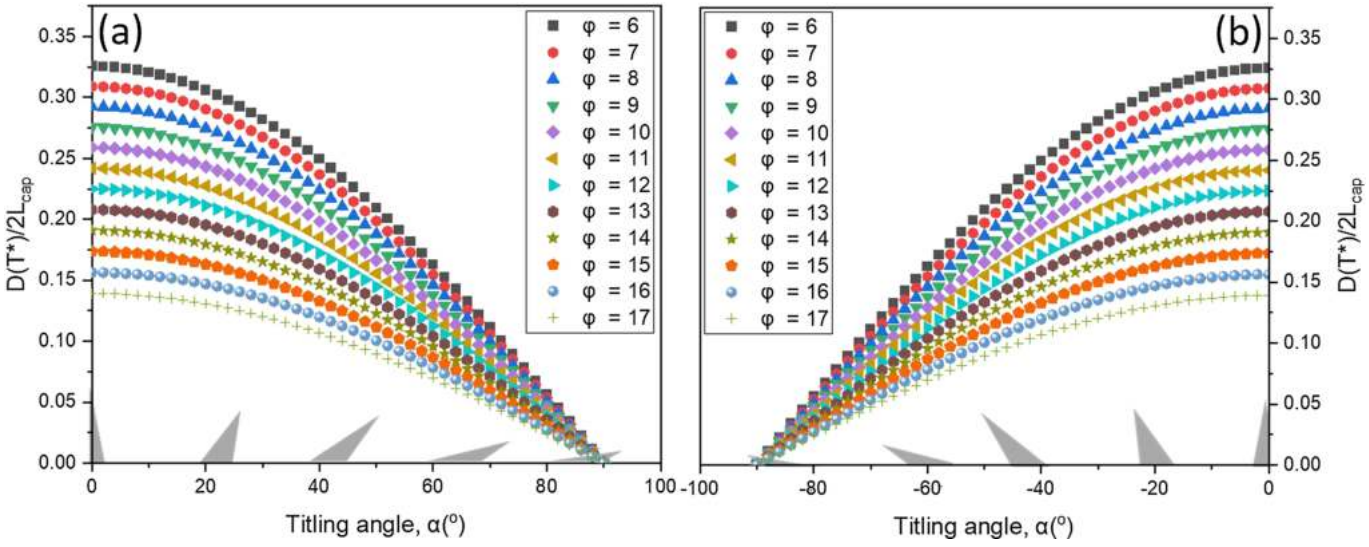

Fig. 5. (a-b) Relative robustness angle parameter T* at various α and φ.

spines from C8/TiO_2-CRM were obtained by analyzing 50 independent nanorods through SEM (See **Fig. S2**). When α varies from −90° to +90°, and φ varies from 6° to 17°, T* always shows a positive value, as shown in Fig. 5**(a-b)**. The composite satisfies ($0 < \theta_o - \frac{\pi}{2} - \varphi < \pi$), considering the contact angle on a smooth surface (θ_o) of C8 (basis: glass as a substrate, C8-GL) is 115° (see Fig. 3**(a-b)**), and thus exhibiting an advantage of forming a robust composite superhydrophobic surface.

Fig. 5**(a-b)** shows that hierarchically structured TiO_2 microflowers

can enhance the stability of the Cassie-Baxter state. The enhancement was due to the fact that hierarchical structure provides more geometries - nanorods branched out into multi arms normal to the plane surface over a wide range of tilt angles (α), thereby creating more local energy barriers to prevent the spreading of liquid. Moreover, pores and grains with a single scale of texture provide less resistance against liquid propagation because the local energy barrier is only at one length scale. Moreover, from Fig. 5**(a-b)**, it can be seen that the decrease of the robustness of a composite is also associated with the increase of the half opening angle φ. This finding is in line with the hypotheses from previous studies [35,42] that suggested that when the local geometric angle of the texture increases (in this work, due to the increase of φ), the net traction on the liquid-vapour interface will favour the downward direction. Since TiO_2 microflowers have relatively uniform and narrow shapes for the half opening angle of the spine around of 11.10° ± 2.3, and were further coated with C8 ($\theta_o = 115°$), their T* was positive, as shown in Fig. 5**(a-b)**. Meanwhile, the robustness parameter H* (see Equation (2)) - taking the striped electro-spun fiber structure as an example - is strongly dependent on the radius (R) of a structure's composite interface. Specifically, H* increases by increasing R. It is postulated that because the size of TiO_2 microflowers is larger than the size of the primary structure of pores and grain, the TiO_2 microflowers surface can achieve higher H*, allowing the C8/TiO_2-CRM to trap more air at the composite interface than the C8-CRM.

$$H^* = \frac{L_{cap} R(1 - cos\theta)}{D^2} \quad (2)$$

3.3. Physico-chemical properties

The functionalization of C8 to hierarchical TiO_2 microflowers-modified ceramic substrate reduces its surface energy. The roughness provided by the TiO_2 microflowers is vital to reducing the contact area between liquid and solid at the interface. Since the bonds of inorganic materials are close and overlap, it is difficult to distinguish them, especially on C8/TiO_2-CRM samples. To address the issue, ATR-FTIR analysis of C8-TiO_2 micro-flowers layer and ceramic substrate was performed independently. The interpretation of the ATR-FTIR spectra confirms the successful C8 grafting over TiO_2 micro-flowers, as shown in Fig. 6(a)**.** The Ti-O-Ti network of the rutile structure of the bond vibration have absorption bands between 505 and 580 cm^{-1} [43,44], and this is corroborated by the sharp and intense band at 700 cm^{-1} (Ti-O-Ti characteristic vibration band) [43]. The peaks at 1147, 1200 and 1245 cm^{-1} for the C8-TiO_2 microflowers are attributed to the fluorocarbon (CF_2 and CF_3) [45,46]. For the ceramic substrate, the peaks show the typical spectrum of alumino-silicate based ceramic. We observe the typical absorption peak of Si-O-Si bond appearing at 1080 cm^{-1} [47]. The peaks at about 790, 737, 830 and 903 cm^{-1} can be attributed to the Si-O-Al bonds [47,48]. The growth of hierarchical TiO_2 microflowers is essential to increase the surface roughness of the ceramic surface to provide multi-level barrier, thus reducing the attraction between liquid and the ceramic surface. The AFM images confirm the presence of micrometer-scale roughness associated with the TiO_2 microflowers layer (Fig. 6(c)). The roughness average (R_a) of the surface demonstrates that, when compared to an untreated ceramic surface (R_a = 0.18 μm) (Fig. 6 (b)), growing TiO_2 microflowers on it via hydrothermal treatment has increased its roughness (R_a = 0.29 μm). The successful surface modification of C8-TiO_2 on the ceramic membrane surface was also demonstrated by the XPS measurement, as shown in Fig. 6. Under hydrothermal conditions, the abundant hydroxyl groups on the ceramic membrane surface allowed for TiO_2 deposition and continued hydroxylation of titanium complex, Ti4 + precursors, resulting in TiO_2 crystallization. The Ti 2p spectrum (Fig. 7(a)) is divided into five typical peaks with respect to Ti, Ti^+, Ti^{2+}, Ti^{3+} and Ti^{4+}. C8 was then subsequently grafted on TiO_2 modified ceramic membrane surface to reduce the surface energy. The curved fits in the fine spectra of the O1s region (Fig. 7(b)) show the formation of Ti-O-Ti, Si-O-Si, and Si-O-Ti bonds, confirming the successful TiO_2 deposition and grafting of C8 to TiO_2 microflowers. The curve fits of (Fig. 7(c)) show a stronger F1s peak, meanwhile the curve fits C1s shows the highest peak at around 292 eV in Fig. 7(d), which is attributed to C-F_2 because it is the main chemical group of C8. The C1s spectrum is fitted with other four characteristic peaks at 285 eV, 286.5 eV, 289 eV and 294 eV, which are assigned to C-C, C-O, C-F and C-F_3, respectively.

3.4. Contact angle analysis with low surface tension liquid

The contact angle of C8/TiO_2-CRM with various low surface tension liquids over a longer contact time period was compared to C8-CRM to gain a better understanding of the effect of hierarchical structure on the surface wettability with low surface tension liquid. The time-dependent variation of droplet contact angles for water, ethylene glycol, and palm oil on two different substrates at room temperature is depicted in Fig. 8. Even though the water droplet evaporates over time, its contact angle C8/TiO_2-CRM is constant over most of the evaporation period (contact angle decreases less than 10° over 30 min, compared to the C8-CRM contact angle decrease of more than 35° over the same timespan). This can be attributed to the membrane's minimal contact angle hysteresis. Moreover, even after 30 min of droplet exposure on the surface of C8/TiO_2-CRM, the water droplet retained its perfect spherical shape (Fig. 9(b)), despite a droplet volume reduction from evaporation (Fig. 9 **(a-b)**).

As shown in Fig. 8(a), the contact angle of the water droplet on the

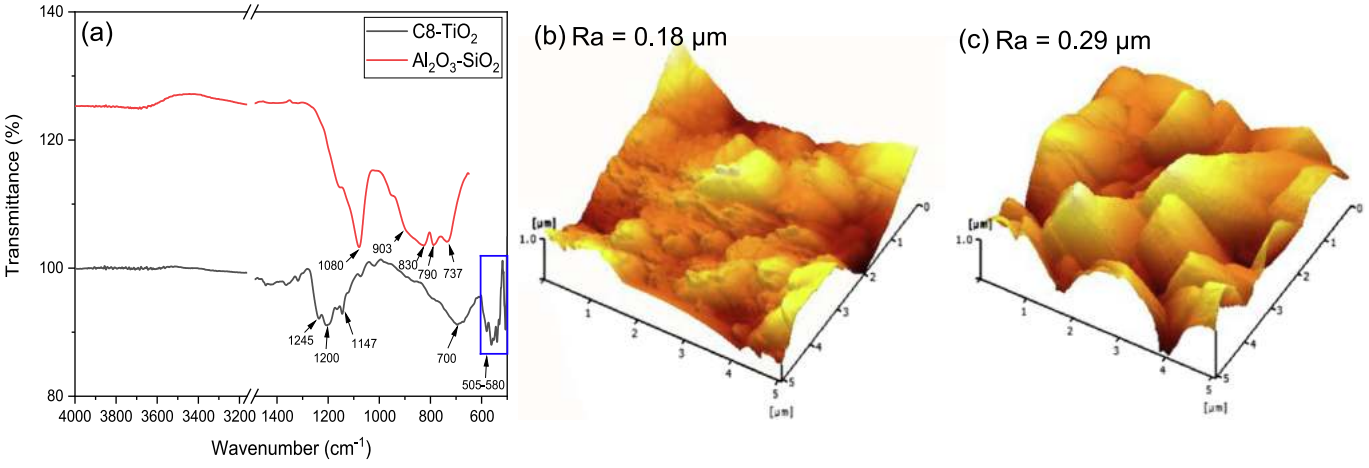

Fig. 6. (a) ATR-FTIR analysis of C8-TiO_2 layer and ceramic substrate and AFM of surface of (b) C8-CRM and (c) C8/TiO_2-CRM.

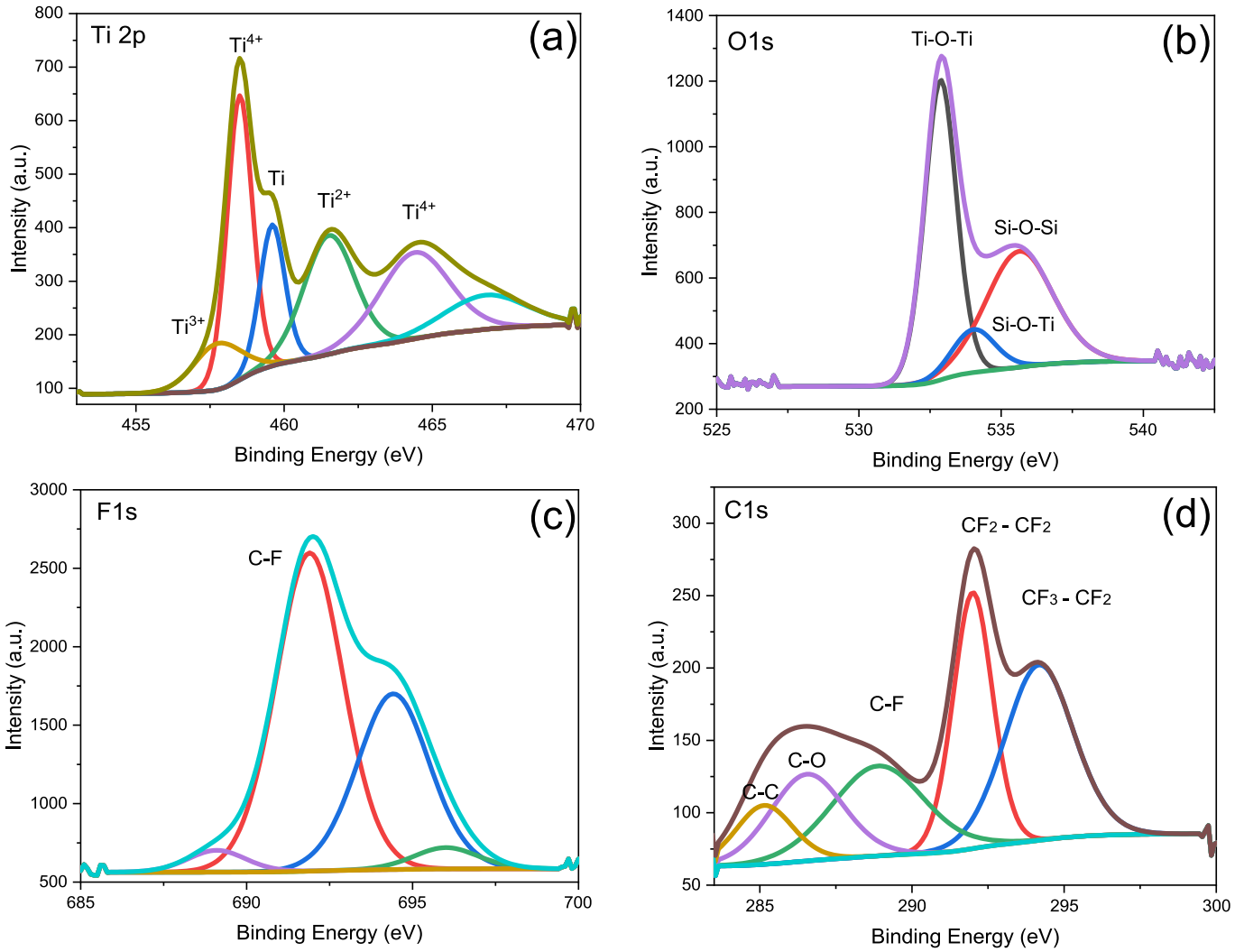

Fig. 7. XPS scan spectra, (a) a fine spectra of F 1s region, (b) a fine spectra of C1s region (c) a fine spectra of O1s region and (d) a fine spectra of Ti2p region of the C8/TiO_2-CRM.

C8-CRM decreases continuously as the droplet evaporate. Within 30 min, the water contact angle on the membrane surface decreases from an average initial contact angle of 136.6° to 101.4°. The complementary roles of the microstructure and nanostructure of flower-like TiO_2 can further increase the apparent contact angle and reduce the contact angle hysteresis (resistance to droplet movement) of the composite. This is due to the fact that air is trapped at multiple length scales for a hierarchically textured surface, as opposed to only one length scale for a single-tiered textured surface. This means that the solid-liquid contact area for hierarchically textured surfaces is reduced even further, thereby, the tendency for droplet spreading is minimized.

Ethylene glycol and palm oil were used to test the wettability of C8-CRM and C8/TiO_2-CRM against those low surface tension liquids. Interestingly, in addition to its extremely superhydrophobic properties, the as-prepared C8/TiO_2-CRM demonstrated excellent ethylene glycol and oil repellency over a relatively long period of time. As illustrated in Fig. 8**(b-c)**, C8/TiO_2-CRM demonstrated a highly stable ethylene and oil contact angle after 40 min. There is a gradual decrease in ethylene glycol and oil contact angle within the first 15 min, but, from then on, their contact angle is purely in a constant contact angle mode, which can represent the receding contact angle. On the contrary, despite exhibiting a stable ethylene glycol contact angle for a long time, the C8-CRM demonstrated a dramatic reduction in oil contact angle within 40 min. The roughness on the surface of C8-CRM caused by grain and pore structures is inadequate to create a sufficient number of voids or air pockets to prevent the intrusion of a liquid with a very low surface tension oil. Meanwhile, the secondary structure of TiO_2 microflowers on the surface of C8/TiO_2-CRM is capable of creating a large number of voids or air pockets, endowing this TiO_2 microflowers with extreme superhydrophobicity.

3.5. *Self-cleaning and anti-fouling study*

The self-cleaning tests of C8-CRM and C8/TiO_2-CRM surfaces are presented graphically in Fig. 10. On the C8-CRM's surface, the water droplets spread and pinned on the entire surface and this pinning behavior is highly associated with Wenzel behavior. On the other hand, water droplets are highly mobile without wetting the surface of C8/TiO_2-CRM, indicating that the surface is in a Cassie-Baxter state. This condition is necessary to create low adhesion and high liquid-repellency surfaces, where a droplet can easily roll off on a substrate. We also carried out a dirt-removal test on the C8-CRM and C8/TiO_2-CRM by dispersing dirt (PMMA powder) partly on their surface. The dirt-removal property was tested simply by passing water over the surface as shown in Fig. 10**(c-d)**. When water was dropped on the dirt-contaminated C8//TiO_2-CRM surface, the droplets trapped and carried the dirt away, leaving a clean surface. Meanwhile, when the water was dropped on the surface of C8-CRM, the droplet pinned and the dirt could not be

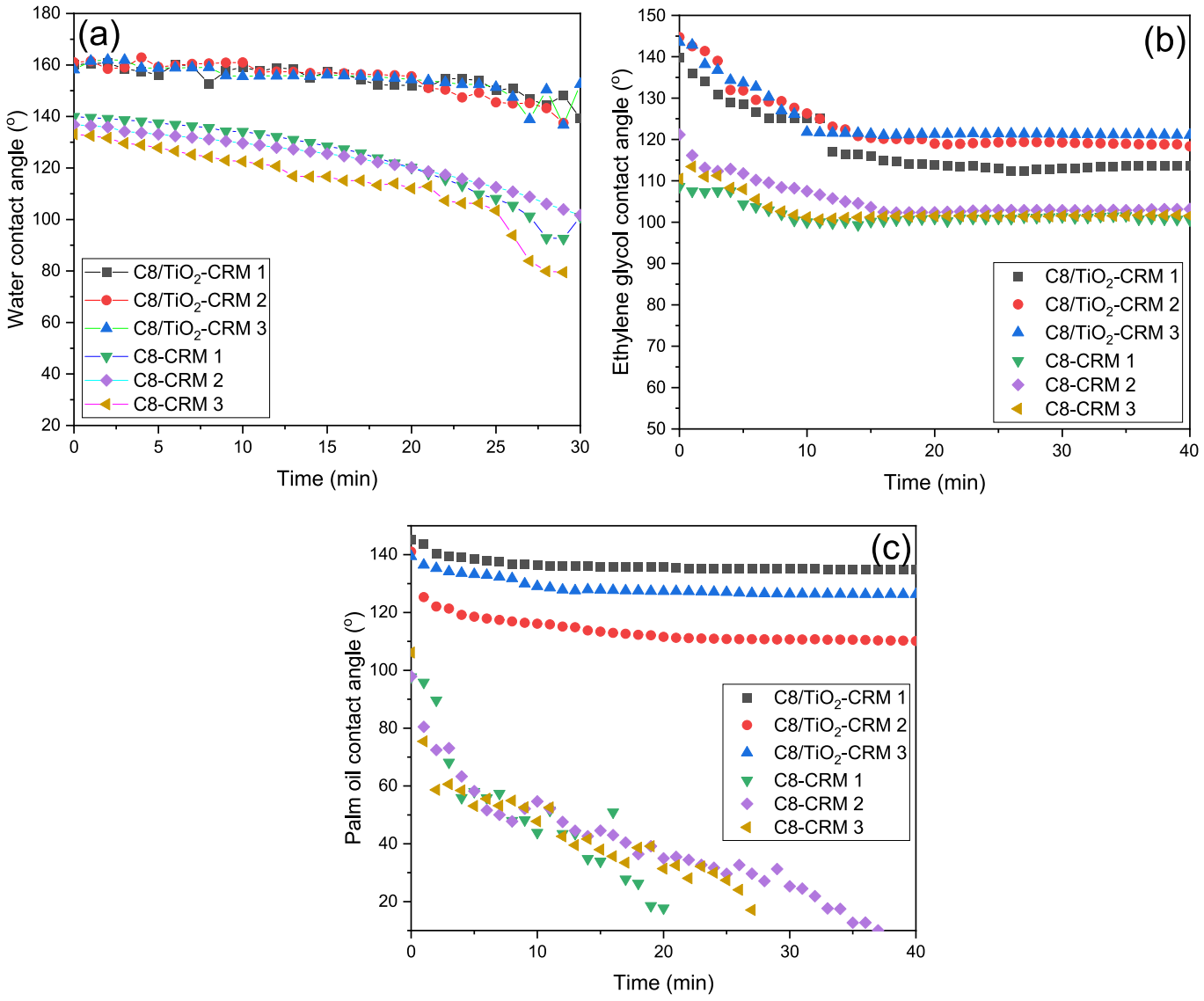

Fig. 8. (a) Water contact angle, (b) ethylene glycol contact angle and (c) palm oil contact angle of C8-CRM and C8/TiO_2-CRM. C8/TiO_2-CRM 1, 2, 3 and C8-CRM 1, 2, 3 in the figure denoted three samples were tested.

effectively removed. Fig. 11 shows EDX analysis on both C8-CRM and C8/TiO_2-CRM after 24 h of immersion in a 10 ppm methylene blue aqueous solution. In comparison to C8/TiO_2-CRM, the surface of contaminated C8-CRM has a higher C content and a lower F content, revealing that there were more foulants on the surface of C8-CRM than C8/TiO_2-CRM.

3.6. Analysis of plastron properties

A hierarchical structure with micro/nano-roughness can aid in the trapping of air beneath liquid, and such a system can promote gas-attracting behavior. To explore such "gasphilic" properties, the bubble gas interaction with C8-CRM and C8/TiO_2-CRM was carried out by immersing them in water. Fig. 12 shows the gasphilic behavior of both samples with air in water. For C8/TiO_2-CRM samples, we observed an instantaneous reduction in air bubble contact angle, and the droplets are completely adsorbed within nearly 2 min. However, in the case of the C8-CRM, the air droplet contact angle remained nearly constant at 80° after 8 min of observation. This phenomenon was also observed by Khan et al [49]. They demonstrated gasphilic surfaces by bubbling CO_2 gas on their textured silicon surfaces, and the gas quickly spread into a sheet of plastron, but a substrate with no plastron bounced off the bubble. Since the trapped air between the solid and liquid is surface area dependent, thereby, the surface area of C8-CRM and C8/TiO_2-CRM was further evaluated via BET analysis. Fig. 12(b) shows the BET surface area of the C8-CRM and C8/TiO_2-CRM. The C8/TiO_2-CRM had surface area of 4.33 m^2/g which was higher than the C8-CRM (0.25 m^2/g). It implies that the composite ceramic surface with hierarchical micro/nano-patterned structures (TiO_2 microflowers) had approximately 17 times the surface area of the C8-CRM, allowing for more area for gas trapping. The C8/TiO_2-CRM exhibits not only superhydrophobicity in air but also gas-philicity in water, indicating that this superhydrophobic coating has a wide range of potential applications in many ceramic fields for gas adsorption.

4. Conclusion

In conclusion, TiO_2 microflowers with relatively uniform and narrow shapes for the half opening angle of the spine around of 11.10° ± 2.3 and coated with C8 ($\theta_o = 115°$) resulted in a robust anti-wetting surface as the T* was found to be positive. Moreover, the micro-size of TiO_2 microflowers plays a major role in achieving higher H*, allowing the

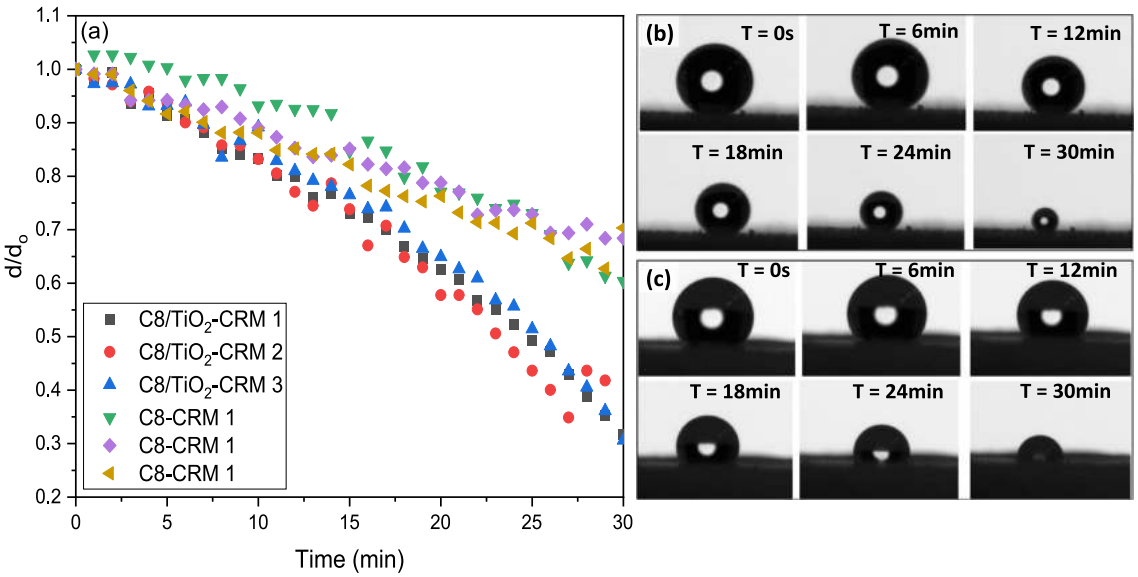

Fig. 9. (a) Nondimensional droplet diameter (d/d_o) with respect to time on the C8/TiO_2-CRM and C8-CRM. Contact diameter, d is normalized with respect to the initial droplet diameter, d_o. C8/TiO_2-CRM 1, 2, 3 and C8-CRM 1, 2, 3 in the figure denoted three samples were tested. Image of water droplet evaporation on (b) C8/TiO_2-CRM and (c) C8-CRM within 30 min.

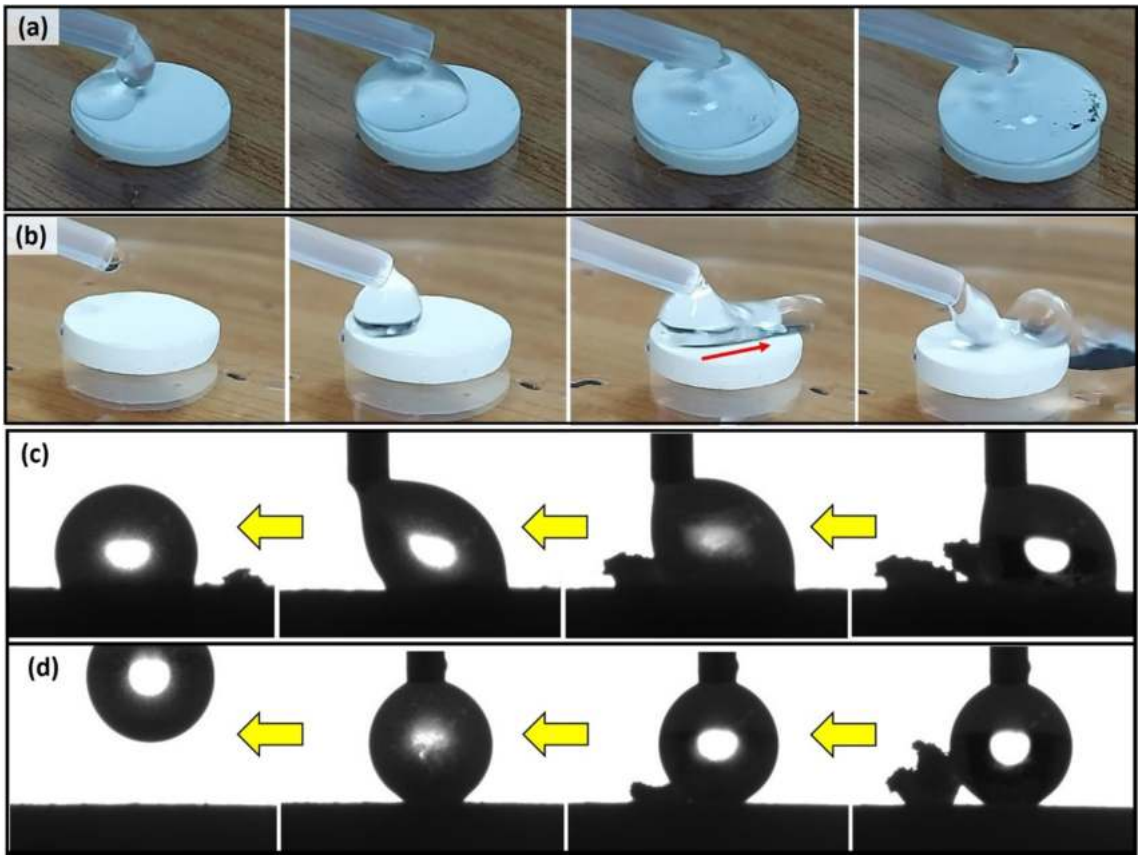

Fig. 10. (a) Water droplet pinned and (b) roll-off on the surface of C8-CRM and C8/TiO_2-CRM respectively. A dirt-removal test on the (c) C8-CRM and (d) C8/TiO_2-CRM by putting PMMA powder as dirt.

C8/TiO_2-CRM to trap more air at the composite interface. Based on contact angle analysis, the geometry of the hierarchical TiO_2 micro-flower led to high Cassie-State stability towards water and also high liquid repellency against palm oil and ethylene glycol. The structures provide more local energy barriers to prevent the spreading of liquid. Meanwhile, because the local energy barrier from pores and grains is only at one length scale, the surface of the ceramic substrate with no secondary structure is completely wetted with oil. The C8/TiO_2-CRM also had better self-cleaning properties than the C8-CRM because the water droplet can easily roll off its surface as opposed to the C8-CRM,

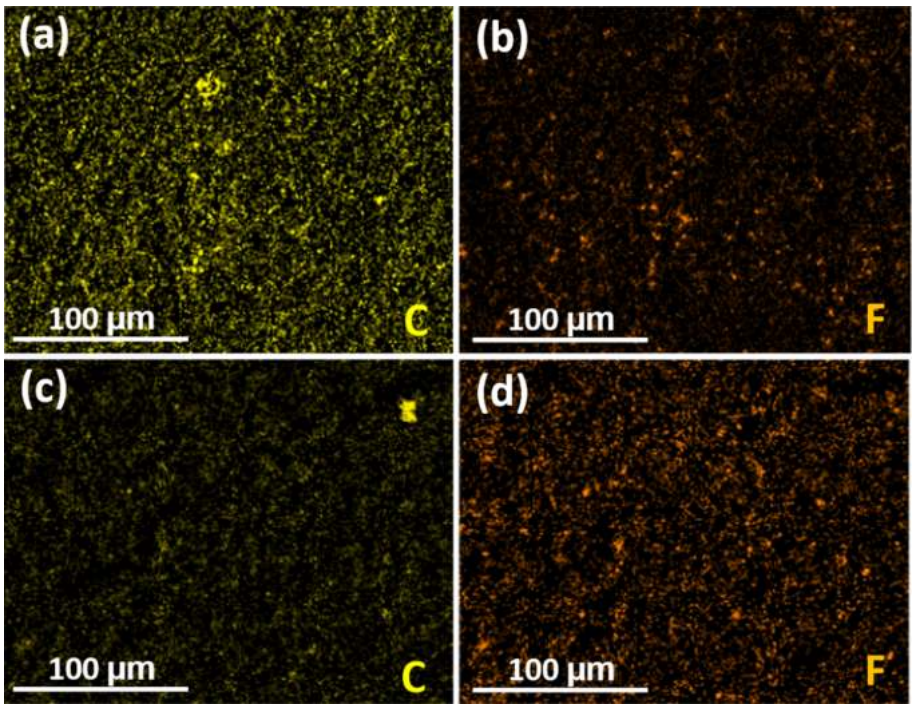

Fig. 11. EDX analysis of elemental composition of (a-b) C8-CRM and (c-d) C8/TiO_2-CRM surfaces after 24 h of immersion in a 10 ppm methylene blue aqueous solution.

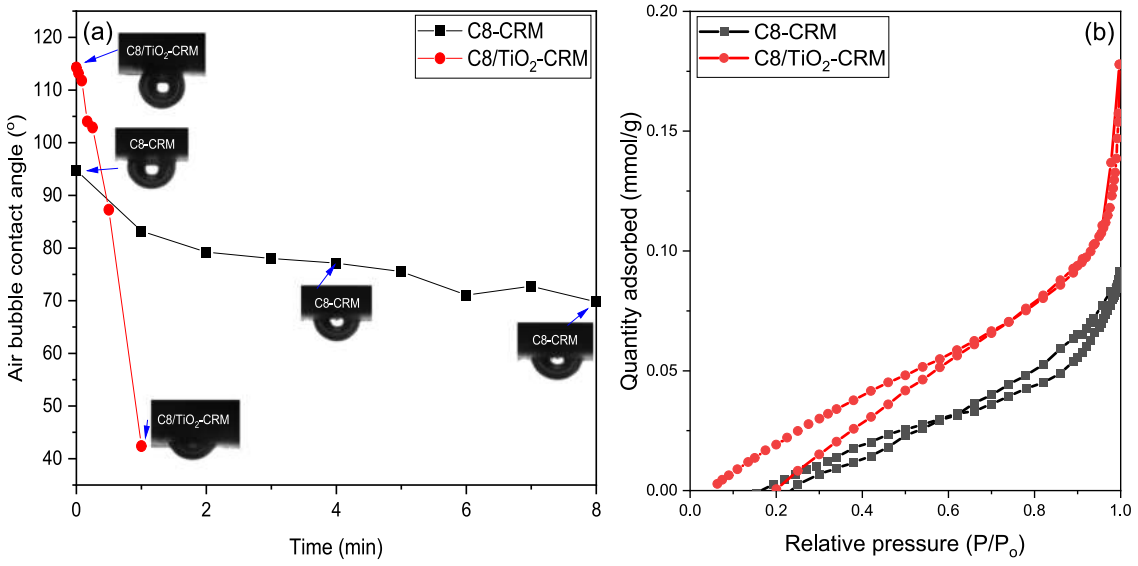

Fig. 12. (a) Air droplet in water contact angle analysis on the submerged C8-CRM and C8/TiO_2-CRM and (b) BET analysis of the surface area of C8-CRM and C8/TiO_2-CRM.

where the water droplet is pinned. In addition, the C8/TiO_2-CRM also exhibited better anti-fouling properties than C8-CRM when immersing them into a 10 ppm methylene blue aqueous solution for 24 h. The C8/TiO_2-CRM structure is not only superhydrophobic in air, but also gasphilic when immersed in water. We discovered that the micro/nanoroughness of TiO_2 microflowers can promote gas-attracting behavior, possibly due to the trapping of air beneath liquid. Moreover, based on the water, ethylene glycol and palm oil contact angle results, it is safe to conclude that a ceramic substrate with a stable superhydrophobicity was achieved with potential oleophobicity by designing a multiscale surface through deposition of TiO_2 microflowers and lowering its surface energy via fluorination. It is worth noting that the implementation of a multi-scale texture surface was carried out in this work at a single step of hydrothermal synthesis, overcoming many previous strategies that primarily involved multiple steps in depositing a nanoscale texture on an underlying coarser length scale texture. Initial speculation could be that this gas-attracting property is highly advantageous for applications like membrane contactor, carbon capture, battery technology, electrocatalytic reduction and so-forth.

CRediT authorship contribution statement

Mohd Haiqal Abd Aziz: Data curation, Writing – original draft, Conceptualization, Methodology, Formal analysis, Investigation,

Writing – review & editing, Validation. **Mohd Hafiz Dzarfan Othman:** Supervision, Writing – original draft, Conceptualization, Methodology, Investigation, Resources, Funding acquisition, Validation, Project administration, Writing – review & editing. **Jason R. Tavares:** Writing – review & editing, Supervision, Resources. **Mohammad Arif Budiman Pauzan:** Methodology, Investigation, Writing – review & editing. **Mizuki Tenjimbayashi:** Writing – review & editing. **Ang Wei Lun:** Writing – review & editing. **Nur Hashimah Alias:** Writing – review & editing, Resources. **Ahmad Fauzi Ismail:** Writing – review & editing, Resources. **Mukhlis A. Rahman:** Writing – review & editing, Resources. **Juhana Jaafar:** Writing – review & editing, Resources.

Declaration of Competing Interest

The authors declare that they have no known competing financial interests or personal relationships that could have appeared to influence the work reported in this paper.

Acknowledgements

The authors gratefully acknowledge the financial support from the Ministry of Science, Technology and Innovation (MOSTI) Malaysia through International Collabortion Fund (ICF) grant (Project Number: IF0120I1164/R.J130000.4909.4S145), Ministry of Higher Education Malaysia under Higher Institution Centre of Excellence (HICoE) grant (Project Number: R.J090301.7809.4J430) and Universiti Teknologi Malaysia under Matching Grant (Project Number: Q. J130000.3009.03M15).

The author also would like to thank The Canada-ASEAN Scholarships and Educational Exchanges for Development (SEED) program. The authors would also like to acknowledge the postdoctoral research scheme (Modal Insan (RGA1)).

Appendix A. Supplementary material

Supplementary data to this article can be found online at https://doi.org/10.1016/j.apsusc.2022.153702.

References

[1] Y. Liao, G. Zheng, J.J. Huang, M. Tian, R. Wang, Development of robust and superhydrophobic membranes to mitigate membrane scaling and fouling in membrane distillation, J. Memb. Sci. 601 (2020) 117962, https://doi.org/10.1016/j.memsci.2020.117962.

[2] Z. Xiao, Z. Li, H. Guo, Y. Liu, Y. Wang, H. Yin, Scaling mitigation in membrane distillation : From superhydrophobic to slippery, Desalination 466 (2019) 36–43, https://doi.org/10.1016/j.desal.2019.05.006.

[3] D. Hou, K.S.S. Christie, K. Wang, M. Tang, D. Wang, J. Wang, Biomimetic superhydrophobic membrane for membrane distillation with robust wetting and fouling resistance, J. Memb. Sci. 599 (2020) 117708, https://doi.org/10.1016/j.memsci.2019.117708.

[4] C. Su, T. Horseman, H. Cao, K. Christie, Y. Li, S. Lin, Robust Superhydrophobic Membrane for Membrane Distillation with Excellent Scaling Resistance, Environ. Sci. Technol. 53 (20) (2019) 11801–11809, https://doi.org/10.1021/acs.est.9b04362.

[5] J.A. Kharraz, A.K. An, Patterned Superhydrophobic Polyvinylidene Fluoride (PVDF) Membranes for Membrane Distillation : Enhanced Flux with improved Fouling and Wetting Resistance, J. Memb. Sci. 595 (2020), 117596, https://doi.org/10.1016/j.memsci.2019.117596.

[6] X. Zhao, D.S. Park, J. Choi, S. Park, S.A. Soper, M.C. Murphy, Flexible-templated imprinting for fluorine-free, omniphobic plastics with re-entrant structures, J. Colloid Interface Sci. 585 (2021) 668–675, https://doi.org/10.1016/j.jcis.2020.10.046.

[7] X. Gou, Z. Guo, Surface topographies of biomimetic superamphiphobic materials : design criteria, fabrication and performance, Adv. Colloid Interface Sci. 269 (2019) 87–121, https://doi.org/10.1016/j.cis.2019.04.007.

[8] C. Bruel, S. Queffeulou, T. Darlow, N. Virgilio, J.R. Tavares, G.S. Patience, Experimental methods in chemical engineering: Contact angles, Can. J. Chem. Eng. 97 (4) (2019) 832–842, https://doi.org/10.1002/cjce.23408.

[9] X. Dai, B.B. Stogin, S. Yang, T. Wong, Slippery Wenzel State, ACS Nano 9 (2015) 9260–9267, https://doi.org/10.1021/acsnano.5b04151.

[10] S. Parvate, P. Dixit, S. Chattopadhyay, Superhydrophobic Surfaces : Insights from Theory and Experiment, J. Phys. Chem. B 124 (2020) 1323–1360, https://doi.org/10.1021/acs.jpcb.9b08567.

[11] H.K. Lee, S.S. Ray, D.T.T. Huyen, W. Kang, Y.-N. Kwon, Chemical and surface engineered superhydrophobic patterned membrane with enhanced wetting and fouling resistance for improved membrane distillation performance, J. Memb. Sci. 629 (2021), 119280, https://doi.org/10.1016/j.memsci.2021.119280.

[12] Y. Liao, R. Wang, A.G. Fane, Engineering superhydrophobic surface on poly (vinylidene fluoride) nanofiber membranes for direct contact membrane distillation, J. Membr. Sci. 440 (2013) 77–87, https://doi.org/10.1016/j.memsci.2013.04.006.

[13] J. Guo, B.J. Deka, K.-J. Kim, A.K. An, Regeneration of superhydrophobic TiO2 electrospun membranes in seawater desalination by water flushing in membrane distillation, Desalination 468 (2019), 114054, https://doi.org/10.1016/j.desal.2019.06.020.

[14] H.-F. Tan, W.-L. Tan, B.S. Ooi, C.P. Leo, Superhydrophobic PVDF/micro fibrillated cellulose membrane for membrane distillation crystallization of struvite, Chem. Eng. Res. Des. 170 (2021) 54–68, https://doi.org/10.1016/j.cherd.2021.03.027.

[15] J. Ju, K. Fejjari, Y. Cheng, M. Liu, Z. Li, W. Kang, Y. Liao, Engineering hierarchically structured superhydrophobic PTFE/POSS nanofibrous membranes for membrane distillation, Desalination 486 (2020) 114481, https://doi.org/10.1016/j.desal.2020.114481.

[16] E. Bittoun, A. Marmur, The Role of Multiscale Roughness in the Lotus Effect: Is It Essential for Super-Hydrophobicity? Langmuir 28 (39) (2012) 13933–13942, https://doi.org/10.1021/la3029512.

[17] T.P.N. Nguyen, R. Boukherroub, V. Thomy, Y. Coffinier, Micro-and nanostructured silicon-based superomniphobic surfaces, J. Colloid Interface Sci. 416 (2014) 280–288, https://doi.org/10.1016/j.jcis.2013.10.065.

[18] Y. Su, B. Ji, K. Zhang, H. Gao, Y. Huang, K. Hwang, Nano to Micro Structural Hierarchy Is Crucial for Stable Superhydrophobic and Water-Repellent Surfaces, Langmuir 26 (7) (2010) 4984–4989, https://doi.org/10.1021/la9036452.

[19] A.K. Kota, G. Kwon, A. Tuteja, The design and applications of superomniphobic surfaces, NPG Asia Mater. 6 (e109) (2014), https://doi.org/10.1038/am.2014.34.

[20] G. Zheng, L. Yao, X. You, Y. Liao, R. Wang, J.J. Huang, Effects of different secondary nano-scaled roughness on the properties of omniphobic membranes for brine treatment using membrane distillation, J. Memb. Sci. 620 (2021), 118918, https://doi.org/10.1016/j.memsci.2020.118918.

[21] Z. Xiao, H. Guo, H. He, Y. Liu, X. Li, Y. Zhang, H. Yin, A.V. Volkov, T. He, Unprecedented scaling/fouling resistance of omniphobic polyvinylidene fluoride membrane with silica nanoparticle coated micropillars in direct contact membrane distillation, J. Memb. Sci. 599 (2020) 117819, https://doi.org/10.1016/j.memsci.2020.117819.

[22] P. Kim, M.J. Kreder, J. Alvarenga, J. Aizenberg, Hierarchical or Not? Effect of the Length Scale and Hierarchy of the Surface Roughness on Omniphobicity of Lubricant-Infused Substrates, Nano Lett. 13 (4) (2013) 1793–1799, https://doi.org/10.1021/nl4003969.

[23] Z.S. Tai, M.H. Abd Aziz, M.H.D. Othman, M.I.H. Mohamed Dzahir, N.A. Hashim, K. N. Koo, S.K. Hubadillah, A.F. Ismail, M.A. Rahman, J. Jaafar, Ceramic Membrane Distillation for Desalination, Sep. Purif. Rev. 49 (4) (2019) 317–356, https://doi.org/10.1080/15422119.2019.1610975.

[24] X. Yu, L. An, J. Yang, S.-T. Tu, J. Yan, CO2 capture using a superhydrophobic ceramic membrane contactor, J. Memb. Sci. 496 (2015) 1–12, https://doi.org/10.1016/j.memsci.2015.08.062.

[25] F. Geyer, C. Schönecker, H.-J. Butt, D. Vollmer, Enhancing CO2 Capture using Robust Superomniphobic Membranes, Adv. Mater. 29 (5) (2017), 1603524, https://doi.org/10.1002/adma.201603524.

[26] C. Li, J. Wei, K.e. Qiu, Y. Wang, Li-air Battery with a Superhydrophobic Li-Protective Layer, ACS Appl. Mater. Interfaces 12 (20) (2020) 23010–23016, https://doi.org/10.1021/acsami.0c05494.

[27] D. Wakerley, S. Lamaison, F. Ozanam, N. Menguy, D. Mercier, P. Marcus, M. Fontecave, V. Mougel, Bio-inspired hydrophobicity promotes CO2 reduction on a Cu surface, Nat. Mater. 18 (2019) 1222–1227, https://doi.org/10.1038/s41563-019-0445-x.

[28] B. Li, Y. Yun, M. Wang, C. Li, W. Yang, J. Li, G. Liu, Superhydrophobic polymer membrane coated by mineralized β -FeOOH nanorods for direct contact membrane distillation, Desalination 500 (2021), 114889, https://doi.org/10.1016/j.desal.2020.114889.

[29] A.T. Hoang, S. Nižetić, X.Q. Duong, L. Rowinski, X.P. Nguyen, Advanced superhydrophobic polymer-based porous absorbents for the treatment of oil-polluted water, Chemosphere 277 (2021) 130274, https://doi.org/10.1016/j.chemosphere.2021.130274.

[30] R. Yamamoto, D. Kowalski, R. Zhu, K. Wada, Y. Sato, S. Kitano, C. Zhu, Y. Aoki, H. Habazaki, Fabrication of superhydrophobic copper metal nanowire surfaces with high thermal conductivity, Appl. Surf. Sci. 537 (2021), https://doi.org/10.1016/j.apsusc.2020.147854.

[31] S.A. Khan, G.S. Boltaev, M. Iqbal, V. Kim, R.A. Ganeev, A.S. Alnaser, Ultrafast fiber laser-induced fabrication of superhydrophobic and self-cleaning metal surfaces, Appl. Surf. Sci. 542 (2021) 148560, https://doi.org/10.1016/j.apsusc.2020.148560.

[32] D. Li, Z. Guo, Metal-organic framework superhydrophobic coating on Kevlar fabric with efficient drag reduction and wear resistance, Appl. Surf. Sci. 443 (2018) 548–557, https://doi.org/10.1016/j.apsusc.2018.03.030.

[33] C.-H. Xue, Q.-Q. Fan, X.-J. Guo, Q.-F. An, S.-T. Jia, Fabrication of superhydrophobic cotton fabrics by grafting of POSS-based polymers on fibers, Appl. Surf. Sci. 465 (2019) 241–248, https://doi.org/10.1016/j.apsusc.2018.09.156.

[34] M.H. Abd Aziz, M.H.D. Othman, N.H. Alias, T. Nakayama, Y. Shingaya, N. A. Hashim, T.A. Kurniawan, T. Matsuura, A.R. Mukhlis, J. Jaafar, Enhanced omniphobicity of mullite hollow fiber membrane with organosilane-functionalized

TiO2 micro-flowers and nanorods layer deposition for desalination using direct contact membrane distillation, J. Memb. Sci. 607 (2020), 118137.
[35] A. Tuteja, W. Choi, J.M. Mabry, G.H. McKinley, R.E. Cohen, Robust omniphobic surfaces, Proc. Nat. Acad. Sci. 105 (47) (2008) 18200–18205, https://doi.org/10.1073/pnas.0804872105.
[36] N.H. Mohtor, M.H.D. Othman, S.A. Bakar, T.A. Kurniawan, H. Dzinun, M.N.A. M. Norddin, Z. Rajis, Synthesis of nanostructured titanium dioxide layer onto kaolin hollow fibre membrane via hydrothermal method for decolourisation of reactive black 5, Chemosphere 208 (2018) 595–605, https://doi.org/10.1016/j.chemosphere.2018.05.159.
[37] S.K. Hubadillah, M.H.D. Othman, T. Matsuura, M.A. Rahman, J. Jaafar, A.F. Ismail, S.Z.M. Amin, Green silica-based ceramic hollow fiber membrane for seawater desalination via direct contact membrane distillation, Sep. Purif. Technol. 205 (2018) 22–31, https://doi.org/10.1016/j.seppur.2018.04.089.
[38] S.K. Hubadillah, M.H.D. Othman, S.H. Sheikh Abdul Kadir, M.R. Jamalluddin, Z. Harun, M.H. Abd Aziz, M. A. Rahman, J. Jaafar, M. Nomura, S. Honda, Y. Iwamoto, H. Fansuri, Removal of As (III) and As (V) from water using green, silica-based ceramic hollow fibre membranes via direct contact membrane distillation, RSC Adv. 9 (2019) 3367–3376, https://doi.org/10.1039/c8ra08143c.
[39] M.I. Siyal, J. Kim, Fluorographite-co-Polydimethylsiloxane coated polyvinylidene-fluoride membrane for desalination of highly saline water with humic acid in direct contact membrane distillation, Environ. Res. 167 (2018) 255–266, https://doi.org/10.1016/j.envres.2018.07.029.
[40] Y.M. Aguilar, J.C. Becerra, R.R. Bertot, J.C. Peláez, G. Liu, C.B. Hurtado, Growth performance, carcass traits and lipid profile of broiler chicks fed with an exogenous emulsifier and increasing levels of energy provided by palm oil, J. Food Agric. Environ. 11 (2013) 629–633.
[41] M. Ye, H.-Y. Liu, C. Lin, Z. Lin, Hierarchical Rutile TiO2 Flower Cluster-Based High Effi ciency Dye-Sensitized Solar Cells via Direct Hydrothermal Growth on Conducting Substrates, Small 9 (2) (2013) 312–321, https://doi.org/10.1002/smll.201201590.
[42] Y. Yamauchi, M. Tenjimbayashi, S. Samitsu, M. Naito, Durable and flexible superhydrophobic materials : abrasion/scratching/slicing/droplet impacting/bending/twisting-tolerant composite with porcupine fish-Like structure, Appl. Mater. Interfaces. 11 (2019) 32381–32389, https://doi.org/10.1021/acsami.9b09524.
[43] Y. Man, L. Mu, Y. Wang, S. Lin, G.L. Rempel, Q. Pan, Synthesis and Characterization of Rutile Titanium Dioxide/Polyacrylate Nanocomposites for Applications in Ultraviolet Light-Shielding Materials, Polym. Compos. 36 (2015) 8–16, https://doi.org/10.1002/pc.22903.
[44] A. Roy, S. Mukhopadhyay, P.S. Devi, S. Sundaram, Polyaniline-layered rutile TiO_2 nanorods as alternative photoanode in dye-sensitized solar cells, ACS Omega 4 (1) (2019) 1130–1138, https://doi.org/10.1021/acsomega.8b02628.
[45] S.M.S. Shahabadi, H. Rabiee, S.M. Seyedi, A. Mokhtare, J.A. Brant, Superhydrophobic dual layer functionalized titanium dioxide/polyvinylidene fluoride-co-hexafluoropropylene (TiO_2/PH) nanofibrous membrane for high flux membrane distillation, J. Memb. Sci. 537 (2017) 140–150, https://doi.org/10.1016/j.memsci.2017.05.039.
[46] D.P. Dowling, C.E. Nwankire, M. Riihimaki, R. Keiski, U. Nylen, Evaluation of the anti-fouling properties of nm thick atmospheric plasma deposited coatings, Surf. Coat. Technol. 205 (5) (2010) 1544–1551, https://doi.org/10.1016/j.surfcoat.2010.10.010.
[47] N.P. Damayanti, Preparation of superhydrophobic PET fabric from Al2O3 – SiO2 hybrid : geometrical approach to create high contact angle surface from low contact angle materials, J. Sol-Gel Sci. Technol. 56 (2010) 47–52, https://doi.org/10.1007/s10971-010-2271-0.
[48] M.H. Abd Aziz, M.H.D. Othman, N.A. Hashim, M.R. Adam, A. Mustafa, Fabrication and characterization of mullite ceramic hollow fiber membrane from natural occurring ball clay, Appl. Clay Sci. 177 (2019) 51–62, https://doi.org/10.1016/j.clay.2019.05.003.
[49] S. Khan, J. Hwang, Y.-S. Horn, K.K. Varanasi, Catalyst-proximal plastrons enhance activity and selectivity of carbon dioxide electroreduction, Cell Rep. Phys. Sci. 2 (2) (2021) 100318, https://doi.org/10.1016/j.xcrp.2020.100318.